Feasibility of seismic time-lapse monitoring of CO_2 with rock physics parametrized full waveform inversion

Qi Hu [1], Dario Grana [2] and Kristopher A. Innanen[1]

[1]*Department of Geoscience, University of Calgary, Calgary, Alberta T2N 1N4, Canada. E-mail: qi.hu1@ucalgary.ca*
[2]*Department of Geology and Geophysics, School of Energy Resources, University of Wyoming, Laramie, WY 82071, USA*

SUMMARY
Carbon capture and storage is an important technology for greenhouse gas mitigation. Monitoring of CO_2 storage should, in addition to locating the plume, provide quantitative information on CO_2 saturation. We propose a full waveform inversion (FWI) algorithm for the prediction of the spatial distribution of CO_2 saturation from time-lapse seismic data. The methodology is based on the application of a rock-physics parametrized FWI scheme that allows for direct updating of reservoir properties. We derive porosity and lithology parameters from baseline data and use them as input to predict CO_2 saturation from monitor data. The method is tested on synthetic time-lapse data generated for the Johansen formation model. Practical issues associated with field data applications, such as acquisition limitations, construction of the initial model, noise and uncertainty in the rock physics model, are taken into account in the simulation. The results demonstrate the robustness of our approach for reconstructing baseline and monitor models. We also illustrate the potential of the approach as compared to conventional two-step inversion algorithms, in which an elastic FWI prediction of velocities and density is followed by rock physics inversion.

Key words: Inverse theory; Numerical approximations and analysis; Waveform inversion.

1 INTRODUCTION

An important technology supporting reduction of greenhouse gas emissions is the geological storage of carbon dioxide (Davis *et al.* 2019; Ringrose 2020; Pörtner *et al.* 2022); for instance, deep saline aquifers have been identified as promising sites for carbon dioxide (CO_2) storage. To ensure and verify the safe geological containment of CO_2 underground, monitoring of CO_2 storage site performance is mandatory (Rütters *et al.* 2013). Injection of CO_2 into the brine-saturated rocks of a saline aquifer changes the elastic moduli, and therefore the seismic response of these media, making seismic a primary technology for monitoring. Time-lapse seismic surveys, in which a series of seismic data sets are acquired at time intervals, provide a monitoring mode in which migration and distribution of the injected CO_2 can be tracked, and leakage problems if any can be identified (Arts *et al.* 2003; Chadwick *et al.* 2005; Romdhane & Querendez 2014; Ghosh *et al.* 2015). Ideally, for reliable conformance verification, quantitative estimates/maps of CO_2 saturation would be produced by such technology, to be compared against reservoir modelling predictions (Dupuy *et al.* 2021a).

Qualitative interpretation of CO_2 from analysis of amplitude changes and time shifts on post-stack seismic images is generally insufficient to understand detailed reservoir conditions (Alemie 2017). Moreover, multiple reflections, interference effects such as tuning, and attenuation introduce ambiguities into seismic images which impede estimation of CO_2 position (Queißer & Singh 2013b; Furre *et al.* 2015). A promising approach to address these issues involves seismic full waveform inversion (FWI), a set of methods with the capacity to produce high-resolution subsurface models, by involving a more complete subset of the information content of seismic data (Tarantola 1986; Brossier *et al.* 2009; Virieux & Operto 2009). FWI, although computationally intensive, in principle accounts for all of these wave propagation effects, and high resolution elastic parameter models (e.g. velocity, density and modulus) derived from FWI can be directly linked to reservoir (or rock physics) properties, such as porosity, fluid saturation and pore pressure. FWI therefore appears to be a potentially powerful tool for quantitative CO_2 characterization and monitoring.

Progress has been reported in managing many of the challenges of practical FWI, which include its computational complexity, dependence on the starting model, sensitivity to incomplete data, etc. (Operto *et al.* 2013; Prieux *et al.* 2013; Métivier *et al.* 2017; Pan *et al.* 2019). Time-lapse FWI faces several additional challenges, not least of which is the need to detect very small changes in the model, changes that are easily obscured by ambient noise, variable near-surface conditions and acquisition non-repeatability (Kamei & Lumley 2017). Efforts have been made to mitigate non-repeatability, through design of monitoring systems (Shulakova *et al.* 2015), data processing strategies

(Roach *et al.* 2015) and inversion strategies (Asnaashari *et al.* 2015; Maharramov *et al.* 2016; Alemie 2017; Kamei & Lumley 2017; Fu *et al.* 2020). As these progress, basic consideration of how to optimally extract critical parameters, especially fluid saturation indicators, becomes increasingly important. In CO_2 storage applications, rock properties are typically extracted sequentially, with the seismic inversion process geared towards determination of elastic properties, from which the actual properties of interest are subsequently determined, often qualitatively (Johnston 2013; Zhang *et al.* 2013). Queißer & Singh (2013a) applied elastic FWI to the Sleipner time-lapse seismic data, and correlated velocity changes with CO_2 saturation changes using the Gassmann's equations; also at Sleipner, Dupuy *et al.* (2017, 2021a) combined acoustic FWI and rock physics inversion to obtain spatial distribution of CO_2 saturation with uncertainty assessment. This aspect of uncertainty quantification is critical for CO_2 storage monitoring as decisions have to be taken based on the monitoring results. However, reports of quantitative, waveform-based CO_2 saturation predictions are uncommon.

The sequential approach itself is neither a necessary, nor always optimal, strategy. The estimation of reservoir properties directly from the seismic data (as opposed to serially, after elastic parameters are first estimated) has several distinct advantages, the main one being that it involves an integrated wave propagation and rock physics formulation, maintaining consistency between elastic and reservoir properties (Doyen 2007; Bosch *et al.* 2010). Inversions of this type can be found in seismic amplitude variation with offset (AVO) settings (Bosch *et al.* 2007; Spikes *et al.* 2007; Grude *et al.* 2013; Liu & Grana 2018; Grana *et al.* 2020), but only very recently have FWI formulations in this mode been examined. Poroelastic FWI (De Barros & Dietrich 2008; Morency *et al.* 2009; Yang *et al.* 2019) moves in this direction, for instance, though the inverse problem is reported to be highly under-determined and ill-posed, and the computational burden very large (Dupuy *et al.* 2021a). Nonetheless, we identify expansion of these efforts as a high priority, in order to take advantage of the more general models available to FWI over AVO (Mallick & Adhikari 2015). Recently, Hu *et al.* (2021) formulated a direct procedure for updating rock and fluid properties within elastic FWI (i.e. EFWI). This was achieved by re-parametrizing the inversion in terms of rock physics properties, adopting a viewpoint similar to that of Russell *et al.* (2011) within an AVO environment. The main advantages of this approach are: (1) it allows examination of any rock physics property that has a well-defined relationship with elastic parameters; (2) it leads to more stable solutions in comparison to those produced through sequential inversion and (3) it shares the same numerical structure as the conventional EFWI. Hu & Innanen (2021) extended the approach to incorporate prior model information.

We have applied the method of Hu *et al.* (2021) to the problem of CO_2 saturation prediction from time-lapse seismic data. To set out the results of these tests, we first review the rock physics FWI framework within which direct rock property updates are calculated, and describe how to apply this approach to time-lapse problems. We then systematically examine the response of the inversion to a synthetic time-lapse data set. Specifically, we recover porosity and lithology parameters from the baseline seismic data, and then use these results as input in the monitor seismic survey, producing estimates of CO_2 saturation. The reliability of the approach is quantified by comparing it to conventional approaches. We end by discussing how uncertainties related to data and rock physics model affect CO_2 saturation reconstructions.

2 METHOD

2.1 Elastic FWI with rock-physics parametrizations

The FWI algorithm we apply is an outgrowth of that set out by Hu & Innanen (2021), which in turn is based on the frequency-domain inversion formulation of Keating & Innanen (2020). We consider isotropic elasticity and a 2-D medium. In the frequency domain, the 2-D elastic wave equations can be written as (Pratt 1990)

$$\omega^2 \rho u + \frac{\partial}{\partial x}\left[(\lambda+2\mu)\frac{\partial u}{\partial x} + \lambda\frac{\partial v}{\partial z}\right] + \frac{\partial}{\partial z}\left[\mu\left(\frac{\partial u}{\partial z} + \frac{\partial v}{\partial x}\right)\right] + f = 0,$$
$$\omega^2 \rho v + \frac{\partial}{\partial z}\left[(\lambda+2\mu)\frac{\partial v}{\partial z} + \lambda\frac{\partial u}{\partial x}\right] + \frac{\partial}{\partial x}\left[\mu\left(\frac{\partial u}{\partial z} + \frac{\partial v}{\partial x}\right)\right] + g = 0, \tag{1}$$

where ω is the angular frequency, ρ is the density, u and v are, respectively, the horizontal and vertical displacements, f and g are the corresponding source terms, and λ and μ are the Lamé parameters. eq. (1) is discretized and solved using the finite-difference equations, which can be formulated in a matrix form

$$\mathbf{Au} = \mathbf{f}, \tag{2}$$

where the coefficients of the impedance matrix $\mathbf{A}$ depend on the frequency and the medium properties, and $\mathbf{u} = (u, v)$ and $\mathbf{f} = (f, g)$ are the vectors containing displacement fields and source terms, respectively. The coefficients within $\mathbf{A}$ are determined by iteratively minimizing the differences between seismic observations $\mathbf{d_{obs}}$, and simulation of data $\mathbf{d_{syn}}$ within model $\mathbf{m} = (m_1, m_2,..., m_n)$. The objective function to be minimized is

$$E(\mathbf{m}) = \frac{1}{2}\Delta\mathbf{d}^t\Delta\mathbf{d}^*, \tag{3}$$

where $\Delta\mathbf{d} = \mathbf{d_{obs}} - \mathbf{d_{syn}}$ contain the data residuals, and the superscripts ^{t} and * denote the transpose and the complex conjugate, respectively. The gradient of E with respect to the ith model variable m_i is Brossier *et al.* (2009)

$$\nabla_{m_i} E = \Re\left\{\mathbf{u}^t\left(\frac{\partial\mathbf{A}}{\partial m_i}\right)^t(\mathbf{A}^{-1})^t\Delta\mathbf{d}^*\right\}. \tag{4}$$

where $\mathfrak{R}$ takes the real part of its argument. The quantity $\partial \mathbf{A}/\partial m_i$ is the scattering radiation pattern associated with model unknown m_i. Within a Newton optimization, the search direction $\delta \mathbf{m}$ for model update is the solution of

$$\mathbf{H}\,\delta \mathbf{m} = -\nabla_{\mathbf{m}} E, \qquad (5)$$

where $\mathbf{H}$ is the Hessian operator. We employ a truncated Gauss Newton method (Métivier *et al.* 2017), in which eq. (5) is solved iteratively, involving only Hessian-vector products.

Let $\mathbf{m} = [m^1, m^2, m^3]$ represent a reference FWI parametrization which is based on three elastic parameters (e.g. the *P*- and *S*-wave velocities plus density) and $\mathbf{r} = [r^1, r^2,..., r^n]$ represent a desired FWI parametrization based on n different rock physics properties, we can express the elastic variables at the ith spatial position as a function of the rock physics variables at the same position: $(m_i^1, m_i^2, m_i^3) = g(r_i^1, r_i^2, ..., r_i^n)$, where g is the rock physics model. From eq. (4), we observe that the elastic variables are altered at each iteration by an update proportional to $\partial \mathbf{A}/m_i$. To transform to the new parametrization $\mathbf{r}$, we compute the chain rule

$$\frac{\partial \mathbf{A}}{\partial r_i^j} = \frac{\partial \mathbf{A}}{\partial m_i^1}\frac{\partial m_i^1}{\partial r_i^j} + \frac{\partial \mathbf{A}}{\partial m_i^2}\frac{\partial m_i^2}{\partial r_i^j} + \frac{\partial \mathbf{A}}{\partial m_i^3}\frac{\partial m_i^3}{\partial r_i^j}, \qquad (6)$$

for each of $j = (1, 2,..., n)$. Given a conventional FWI scheme set up to update variables $\mathbf{m}$, within which the partial derivatives of $\mathbf{A}$ are known, and given the rock physics model g, so that the partial derivatives of $\mathbf{m}$ with respect to $\mathbf{r}$ can be derived, through eq. (6) we can move to a new scheme in which the vector $\mathbf{r}$ is updated.

2.2 Rock physics model

A significant number of rock physics models have been developed, based on experimental data or physical theories or both, to relate the elastic properties of rock to porosity, mineralogy and pore fluid (Mavko *et al.* 2020). We examine a popular rock physics model: the stiff-sand model. This model is widely applied to clay-rich or shaly sandstones and even to shales (Spikes *et al.* 2007; Hossain *et al.* 2011; Grana 2016a; Wawrzyniak-Guz 2019).

The stiff-sand model connects two endpoints in the elastic modulus versus porosity plane. The zero-porosity endpoint has the bulk and shear moduli of the solid phase K_0 and μ_0, which is calculated according to Voigt–Reuss–Hill average (Hill 1952):

$$K_0 = \frac{1}{2}\left[\sum_{i=1}^{N} f_i K_i + \left(\sum_{i=1}^{N} f_i/K_i\right)^{-1}\right], \qquad (7)$$

$$\mu_0 = \frac{1}{2}\left[\sum_{i=1}^{N} f_i \mu_i + \left(\sum_{i=1}^{N} f_i/\mu_i\right)^{-1}\right], \qquad (8)$$

where N is the number of mineral components, f_i, K_i and μ_i are the volume fraction, bulk modulus and shear modulus of the ith mineral component, respectively. Hertz–Mindlin grain-contact theory provides an estimation of the bulk and shear moduli of a dry rock, under the assumption that the rock frame is a random pack of spherical grains, subject to an effective pressure P_e, with a given porosity, and an average number of contacts per grain n (coordination number). In the stiff-sand model, Hertz–Mindlin equations are used to compute the bulk and shear moduli of the dry-rock K_{HM} and μ_{HM} at the critical porosity ϕ_c:

$$K_{HM} = \left[\frac{n^2(1-\phi_c)^2\mu_0^2}{18\pi^2(1-v_0)^2}P_e\right]^{1/3}, \qquad (9)$$

$$\mu_{HM} = \frac{2+3f-v_0(1+3f)}{5(2-v_0)}\left[\frac{3n^2(1-\phi_c)^2\mu_0^2}{2\pi^2(1-v_0)^2}P_e\right]^{1/3}, \qquad (10)$$

where v_0 is the Poisson's ratio of the solid phase, and f is the degree of adhesion between the grains. Then, for porosity $\phi \in (0, \phi_c)$, the bulk and shear moduli K_{dry} and μ_{dry} of the dry-rock are estimated by interpolating the elastic moduli at zero porosity and at critical porosity using the modified Hashin–Shtrikman upper bounds:

$$K_{dry} = \left(\frac{\phi/\phi_c}{K_{HM}+4/3\mu_0} + \frac{1-\phi/\phi_c}{K_0+4/3\mu_0}\right)^{-1} - 4/3\mu_0, \qquad (11)$$

$$\mu_{dry} = \left(\frac{\phi/\phi_c}{\mu_{HM}+\xi} + \frac{1-\phi/\phi_c}{K_0+\xi}\right)^{-1} - \xi, \qquad (12)$$

where

$$\xi = \frac{\mu_0}{6}\frac{9K_0+8\mu_0}{K_0+2\mu_0}. \qquad (13)$$

According to Gassmann's equations, the shear modulus of the saturated rock $\mu_{sat} = \mu_{dry}$, and the bulk modulus of the saturated rock K_{sat} is given by

$$K_{sat} = K_{dry} + \frac{(1-K_{dry}/K_0)^2}{\phi/K_f + (1-\phi)/K_0 - K_{dry}/K_0^2}, \qquad (14)$$

Table 1. Rock physics parameters used in this study.

Parameter	Value	Parameter	Value
Quartz bulk modulus	37 GPa	CO_2 bulk modulus	0.02 GPa
Quartz shear modulus	44 GPa	CO_2 density	0.68 g cm^{-3}
Quartz density	2.65 g cm^{-3}	Effective pressure	0.01 GPa
Clay bulk modulus	25 GPa	Critical porosity	0.4
Clay shear modulus	9 GPa	Coordination number	9
Clay density	2.55 g cm^{-3}	Degree of adhesion	1
Water bulk modulus	2.25 GPa		
Water density	1.03 g cm^{-3}		

where K_f is the fluid bulk modulus. The density of the saturated rock is computed as a weighted average of the densities of mineral and fluid components:

$$\rho = (1 - \phi) \sum_{i=1}^{N} f_i \rho_i + \phi \sum_{i=1}^{M} f_i' \rho_i', \tag{15}$$

where M is the number of fluid components, f_i' is the bulk modulus of the ith fluid component, and ρ_i and ρ_i' are the density of the ith mineral component and the density of the ith fluid component, respectively. The velocities as functions of the elastic moduli and density are then

$$V_{\text{P}} = \sqrt{\frac{K_{\text{sat}} + \frac{4}{3}\mu_{\text{sat}}}{\rho}}, \quad V_{\text{S}} = \sqrt{\frac{\mu_{\text{sat}}}{\rho}}. \tag{16}$$

The partial derivatives of V_{P}, V_{P} and ρ with respect to any rock physics parameters emerging from this model can be calculated. We can then carry out FWI updates of these parameters according to eq. (6).

In this study, we assume two mineral components, quartz and clay, and two fluid components, water and supercritical CO_2. Hence, we define three model unknowns: porosity (ϕ), clay content (C) and CO_2 saturation (Sc). Then, in eq. (15), for instance, we have $N = M = 2, f_1 = C, f_2 = 1 - C, f_1' = Sc$ and $f_2' = 1 - Sc$. The bulk modulus of the two-component fluid is calculated using the Brie *et al.* (1995) equation:

$$K_f = (K_w - K_c)(1 - S_c)^e + K_c \tag{17}$$

where K_w and K_c are the bulk modulus of water and CO_2, respectively. e is the patchiness exponent, with low values (down to 1) corresponding to patchy mixing of fluid phases and high values (up to 40) corresponding to uniform mixing (Dupuy *et al.* 2021a, b). We consider semi-patchy mixing behaviour and use a constant e equal to 5.

Additional rock physics parameters, including the elastic moduli and density of each mineral/fluid component, effective pressure, critical porosity, coordination number and degree of adhesion between the grains, are fixed with the values in Table 1. The modulus and density of CO_2 at temperature 37 °C and pressure 0.01 GPa, given by Mavko *et al.* (2020), are used.

2.3 Time-lapse FWI

Quantitative CO_2 monitoring requires accurate and precise predictions of the CO_2 saturation model at any time at which the data are measured. Although it is possible to jointly invert the three parameters (porosity, clay content and CO_2 saturation) from a single seismic survey, preliminary tests showed that fluid saturation is very difficult to estimate within this parametrization because of the large trade-off between rock physics parameters and its relatively small impact on the data. Here we consider a favourable case by making two assumptions: (1) before CO_2 injection, there is only one fluid component (water) in the subsurface and (2) porosity and lithology parameters are constant in time. Therefore, we propose to estimate the variables sequentially, a strategy similar to that of Grana *et al.* (2020) within a stochastic inversion framework and Dupuy *et al.* (2021a) within an FWI environment. First, we apply the rock physics FWI approach to the baseline (pre-injection) data for the estimation of porosity and clay content; then, we use the same inverse method and use the inverted porosity and clay content models as prior knowledge (fixed values) to estimate CO_2 saturation from monitor (post-injection) data. The objective function for baseline model reconstruction is expressed as

$$E_b = \left\| \mathbf{d}_{\text{obs\_b}}(\phi^t, C^t) - \mathbf{d}_{\text{syn\_b}}(\phi, C) \right\|^2, \tag{18}$$

where $\mathbf{d}_{\text{obs\_b}}$ and $\mathbf{d}_{\text{syn\_b}}$ denote the observed and synthetic baseline data, respectively. ϕ^t and C^t denote the true porosity and clay content models. The baseline CO_2 saturation model is equal to 0 everywhere. The goal is to recover the ϕ and C models by iteratively minimizing the difference between $\mathbf{d}_{\text{obs\_b}}$ and $\mathbf{d}_{\text{syn\_b}}$.

The objective function for monitor model reconstruction is

$$E_m = \left\| \mathbf{d}_{\text{obs\_m}}(\phi^t, C^t, S_{c\_m}^t) - \mathbf{d}_{\text{syn\_m}}(\phi_{\text{inv}}, C_{\text{inv}}, S_{c\_m}) \right\|^2, \tag{19}$$
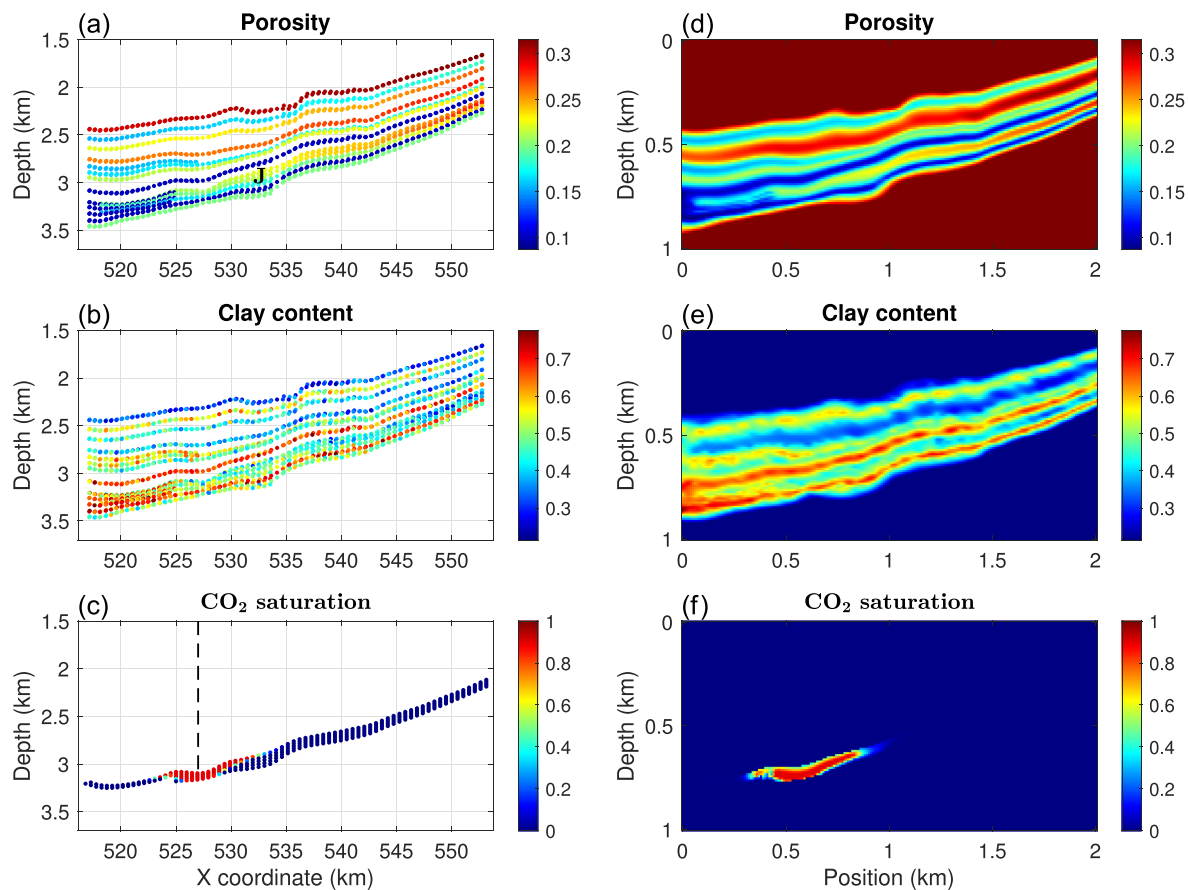
Figure 1. Johansen data set. (a)–(c) Full-field model and (d)–(f) corresponding model that uses a simplified geometry. The letter J indicates the location of the Johansen formation; and the dashed line indicates the location of the injection well.

where $\mathbf{d}_{obs\_m}$ and $\mathbf{d}_{syn\_m}$ are the observed and synthetic monitor data, respectively. ϕ_{inv} and C_{inv} are the inverted porosity and clay content models from the baseline survey. They are not updated in the monitor stage. The goal is to recover the saturation model S_{c_m} by iteratively minimizing the difference between $\mathbf{d}_{obs\_m}$ and $\mathbf{d}_{syn\_m}$.

3 NUMERICAL EXAMPLES

We apply the proposed approach to a synthetic model generated from the Johansen data set. The Johansen formation is a deep saline aquifer located offshore of the south-west coast of Norway. The aquifer is a chosen site for the Northern Lights project, which plans to start operations in mid-2024, for storage of 1.5 million tonnes of CO_2 per year. The MatMoRA project of SINTEF has developed a set of geological models of Johansen based on seismic and well data (Eigestad *et al.* 2009; Bergmo *et al.* 2011). Petrophysical data including porosity and permeability are available.

3.1 Model description

The original full-field model is discretized by a $149 \times 189 \times 16$ grid, with three layers in Johansen. However, we consider 100×16 cells defined on an irregular gird in the vertical direction (Fig. 1a). The uppermost layer situated approximately 600 m above Johansen is the Sognefjord formation, which is the main reservoir for the Troll hydrocarbon field. The low porosity layers above and below Johansen are the Dunlin shale and Amundsen shale, respectively. In particular, the Dunlin shale serves as a cap-rock for the Johansen formation. To account for lithologies of the geomodel, we introduce a clay volume (Fig. 1b) negatively correlated with porosity, with a correlation coefficient of -0.9. Assuming the initial water saturation (before injection) is equal to 1 everywhere, the CO_2 saturation distribution within Johansen (Fig. 1c) was calculated by simulating the fluid flow in year 110, 10 yr after stopping a 100-yr injection with a constant injection rate of $1.4 \times 10^4\,\mathrm{m^3\,d^{-1}}$ (Grana *et al.* 2020).

Because of computational limitations and lack of data, we create a synthetic model with the injection much shallower than in reality and the top and bottom layers of the model are assumed to be homogeneous: first, we define a regular grid and interpolate the original data over the grid. The grid consists of 101×201 node points with a depth increment of 20 m and a position increment of 180 m; second, we change
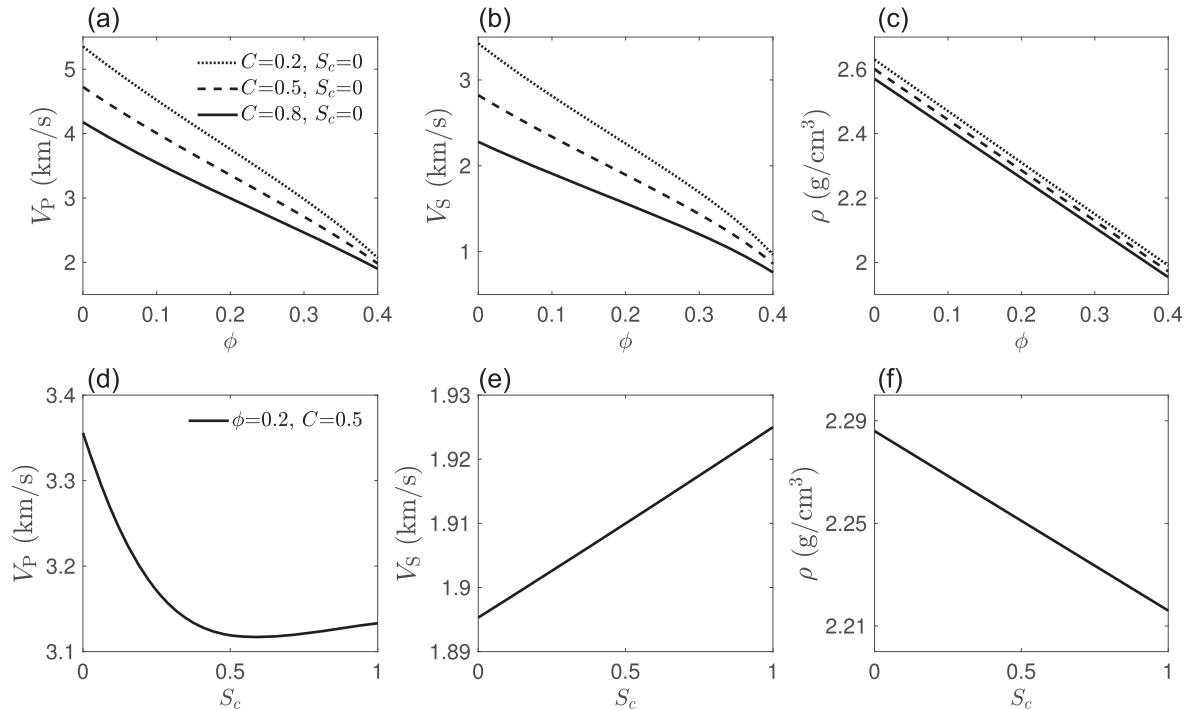
Figure 2. Theoretical curves of the stiff-sand model: *P*-wave velocity, *S*-wave velocity and density versus (a)–(c) porosity and (d)-(f) CO₂ saturation.

the spatial step to 10 m and use relative depth and position. The models in Figs 1(d)–(f) are then used to examine the proposed FWI method. The sandstone reservoir is distinguished by higher porosity and lower clay content values compared to the surrounding shale. Porosity in the reservoir varies between 0.15 and 0.29, with the porosity within a zone degrading towards south as the depth of the formation increases. The initial CO₂ saturation is 0 everywhere and then changes locally due to the injection at 750 m depth. The maximum CO₂ saturation is 0.9.

In Fig. 2, we compute velocities and density as a function of porosity, clay content and CO₂ saturation based on the stiff-sand model. With CO₂ replacing water, the *P*-wave velocity of the saturated rock decreases due to the lower bulk modulus of CO₂, the density decreases due to the lower density of CO₂, and the *S*-wave velocity slightly increases since the fluid only affects the density in the *S*-wave velocity expression. The *P*-wave velocity does not decrease monotonically as CO₂ saturation increases because the relative change in bulk modulus is smaller than that in density when CO₂ saturation is larger than 0.6. It also shows that the sensitivity of the elastic attributes is dominated by porosity and to a lesser degree by clay content and fluid saturation. In Fig. 3, we plot the velocity and density models corresponding to the rock property model (Figs 1d–f). The time-lapse elastic changes are consistent with the analysis in Fig. 2. The fluid effect is also well illustrated in the noise-free synthetic data (Fig. 4).

The inversion experiments are presented in three parts. First, we carry out the direct, rock physics parametrized FWI approach with noise-free data (Fig. 4), and compute the synthetic data in inversion using the same simulation through which the observed data are generated. Then, we repeat the test using conventional two-step inversions, in which velocities and density are first determined through elastic FWI, followed by rock physics properties. These simulations allow us to examine parameter resolution issues and make clear comparisons between the results of direct and two-step inversions. Finally, we take into account two different sources of uncertainty within the direct approach: uncertainty in the data and uncertainty in the rock physics model.

In all tests, we consider a surface acquisition geometry, with 20 explosive sources every 100 m at 20 m depth and 100 receivers every 20 m at 10 m depth. The source signature is assumed to be known. The recorded data are multicomponent displacements. We adopt a multiscale approach (Bunks *et al.* 1995; Brossier *et al.* 2009) by inverting 10 frequency bands, each containing five evenly spaced frequencies from 2 Hz to a maximum frequency; the maximum frequency is 3 Hz for the first band, and it increases to 25 Hz for the last band (following the strategy advocated by Keating & Innanen 2019). A truncated Gauss–Newton optimization method (Métivier *et al.* 2017), comprising 20 inner iterations and 1 outer iteration for each frequency band, is used.

3.2 Direct FWI results

3.2.1 Baseline model reconstruction

One of the challenges of predicting rock physics properties from seismic data is the low-frequency (initial) model. In a typical elastic inversion, the low-frequency model of velocity is often related to models used for seismic processing, for example stacking velocities. In the rock physics domain, a low-frequency model is more challenging to define because different lithologies might have different rock physics
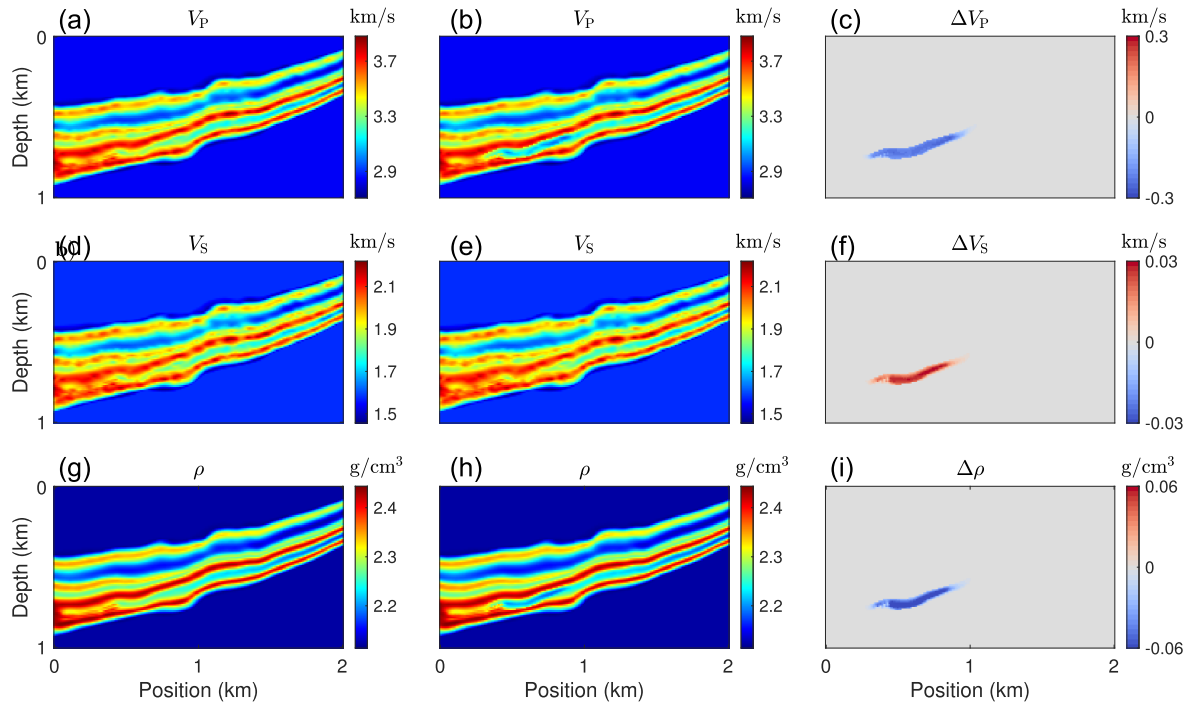
Figure 3. True (a)–(c) baseline, (d)–(f) monitor and (g)–(i) time-lapse models of *P*- and *S*-wave velocities plus density. **(The labels of subfigures, after the edition, are not consistent with the descriptive caption. We prefer the original labels, as showns in figs 12 and 14, namely 'abc' on the left, 'def' on the middle, and 'ghi' on the right)**
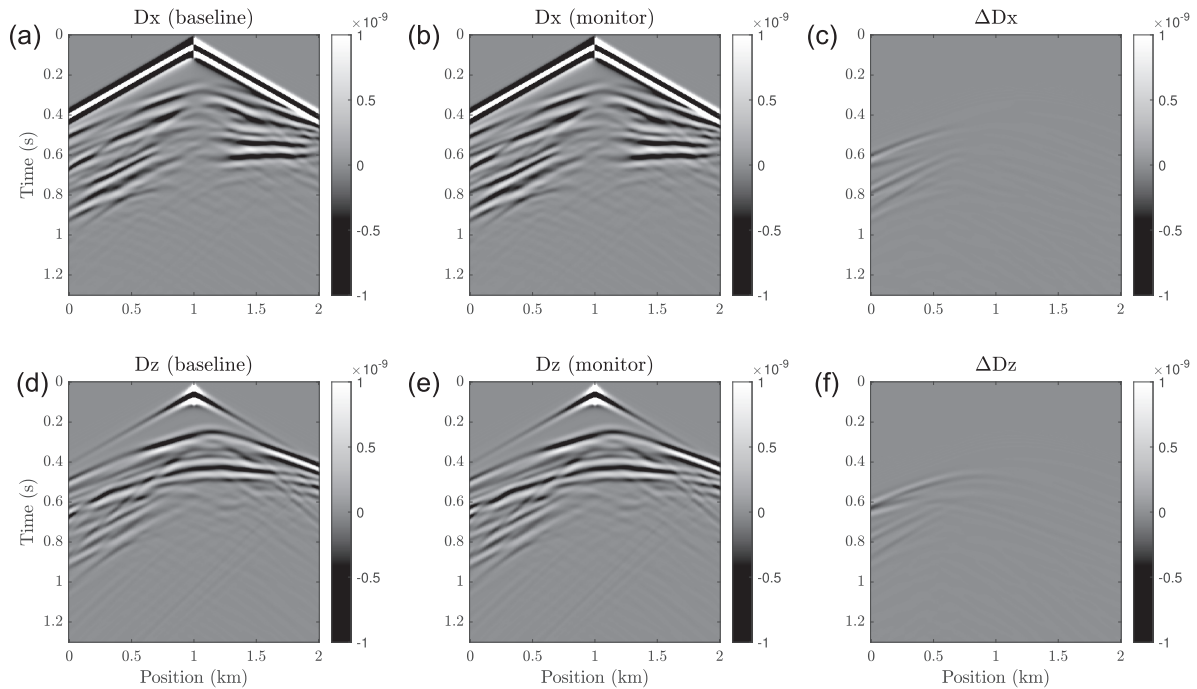

Figure 4. (a) and (d) Baseline, (b) and (e) monitor and (c) and (f) differential seismograms computed for the true model. (a)–(c) Horizontal displacement. (d)–(f) Vertical displacement. The shot is located at lateral position 1 km. Ricker wavelet source with a central frequency of 15 Hz is used.

models (Grana *et al.* 2021). Here we derive the initial porosity and clay models from a filtered *P*-wave velocity model, using regressions of the direct measurements (well log data) of these variables, which are assumed to be available. We use linear regressions because the nonlinearity of the $V_P - \phi$ and $V_P - C$ relationships are not strong (Fig. 5). As a result, the initial models in Figs 6(b) and (c) are used in inversion.

The recovered porosity and clay content models are reasonably accurate, with relatively low resolution near the left edge of the model due to limited observation aperture (Fig. 7). The porosity seems better resolved than clay content thanks to the larger impact of porosity on seismic attributes (Fig. 2). In Fig. 8, the convergence properties of the inversion are summarized. We start iterations at low frequencies to
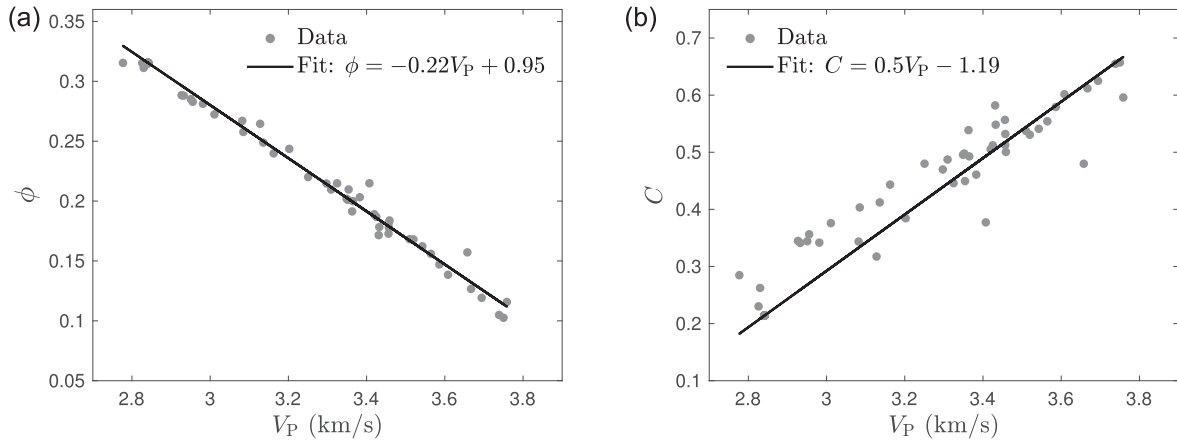
Figure 5. (a) $V_P - \phi$ and (b) $V_P - C$ relationships for constructing the initial ϕ and C models. The data are from the true model (Figs 1d, e and 3a) at lateral position 0.5 km.
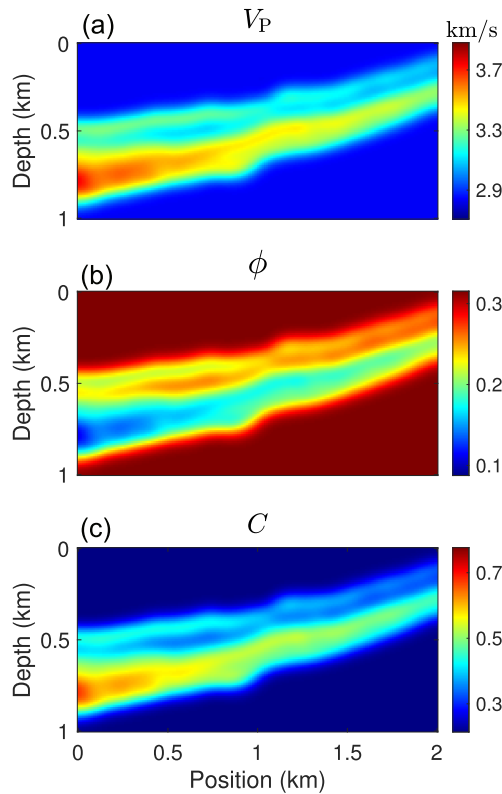

Figure 6. Initial models: (a) *P*-wave velocity, (b) porosity and (c) clay content.

prevent convergence of the objective function toward local minima, and then slowly introduce higher frequencies to image fine structures. The objective function has a sudden increase when entering into a next frequency band, but decreases to close to the original number after model updating. The solutions are examined via the relative model error $\xi = \|\mathbf{m} - \mathbf{m}_t\|_2 / \|\mathbf{m}_0 - \mathbf{m}_t\|_2$, where $\mathbf{m}$, $\mathbf{m}_0$, and $\mathbf{m}_t$ represent the inverted, initial and true models, respectively, so that each model starts its iteration with a unit error. We observe the convergence characteristics of a reliable inversion. The model errors decrease monotonically, with porosity updated more efficiently than clay content. Fig. 9 shows the comparison between the initial and inverted models in terms of the modelled data. The data residual is significantly reduced after inversion.

3.2.2 Monitor model reconstruction

In the monitor survey, the observed data are generated from the true model (Fig. 1); the synthetic data are generated from the recovered baseline model (Fig. 7) plus the current estimate of CO_2 saturation. For the initial guess of CO_2, we interpret the reservoir horizons from baseline estimates and restrict saturation variations within the reservoir. The interpreted horizons do not match exactly the rim of the plume
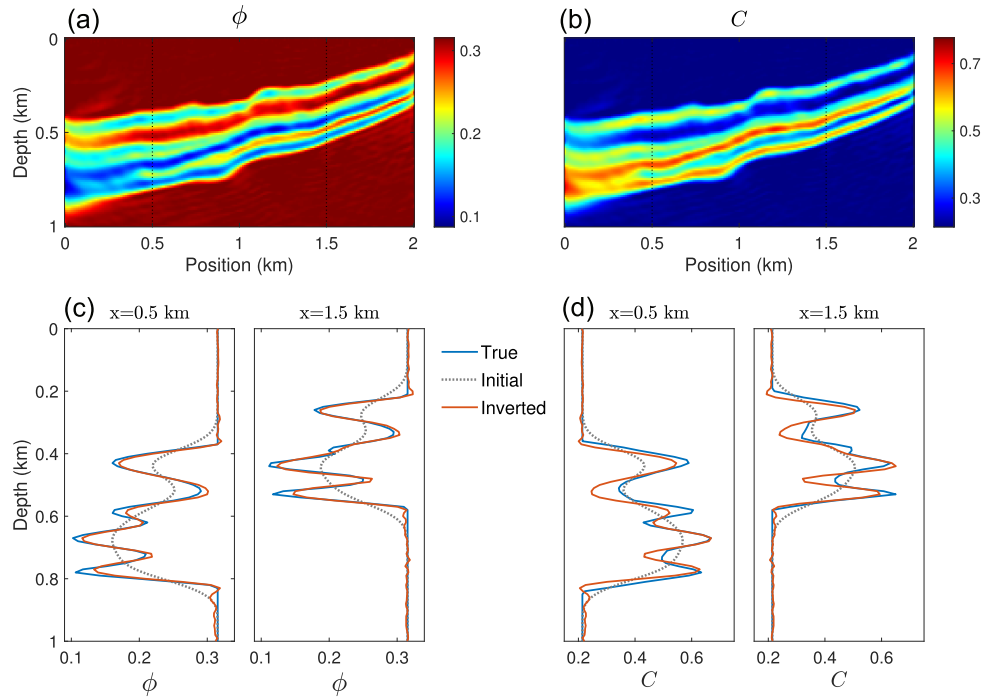
Figure 7. Inverted models: (a) porosity and (b) clay content. (c) and (d) Vertical profiles extracted from the true, initial and inverted models at lateral positions $x = 0.5$ and 1.5 km.
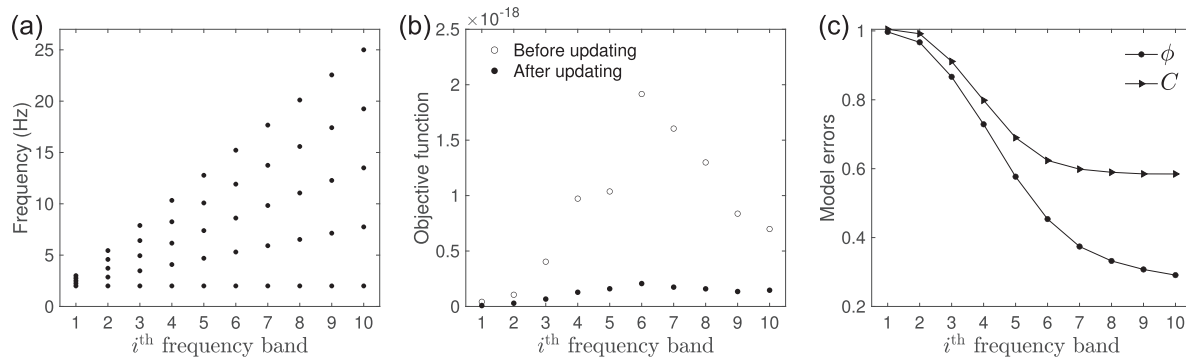

Figure 8. Convergence properties. (a)–(c) Frequencies, objective functions and model errors (after updating) within a frequency band, respectively.

(Fig. 10a), allowing uncertainty related to horizons to be taken into account. Regarding saturation values, we use a Gaussian function varying only in the *x*-direction with a maximum value of 0.9 at the location of the injection well (Fig. 10b). For the inversion, we incorporate the first-order Tikhonov regularization term (Tikhonov & Arsenin 1977; Asnaashari *et al.* 2013) into the objective function, to encourage a small degree of smoothness in the solution. The hyper-parameter is chosen such that the ratio between the regularization term and data misfit is 1 $\times$ 10^{-4} at each iteration. The recovered model (Fig. 10c) shows a good agreement with the true one, with both the spread of the plume and saturation values well estimated. The data residuals corresponding to the initial and inverted models are shown in Fig. 11.

One of the advantages of the direct approach is that it allows elastic attributes to be jointly output with rock physics properties. In Figs 12 and 13, the velocity and density models corresponding to the rock physics estimates (Figs 7 and 10) are summarized. The elastic models are correctly retrieved, in particular, the predicted time-lapse elastic changes match closely the true ones, showing great consistency between the baseline and monitor reconstructions.

3.3 Two-step inversion results

The two-step inversion combines FWI for elastic attributes and rock physics inversion that transforms the elastic attributes to reservoir properties.

For the elastic inversion, we parametrize FWI in terms of *P*- and *S*-wave velocities, and density. We use the parallel difference strategy (Plessix *et al.* 2010; Asnaashari *et al.* 2015) which independently inverts the baseline and monitor data sets (Fig. 4) starting from the same initial model (Fig. 6). The time-lapse variation is simply the subtraction between the recovered monitor model and the recovered baseline
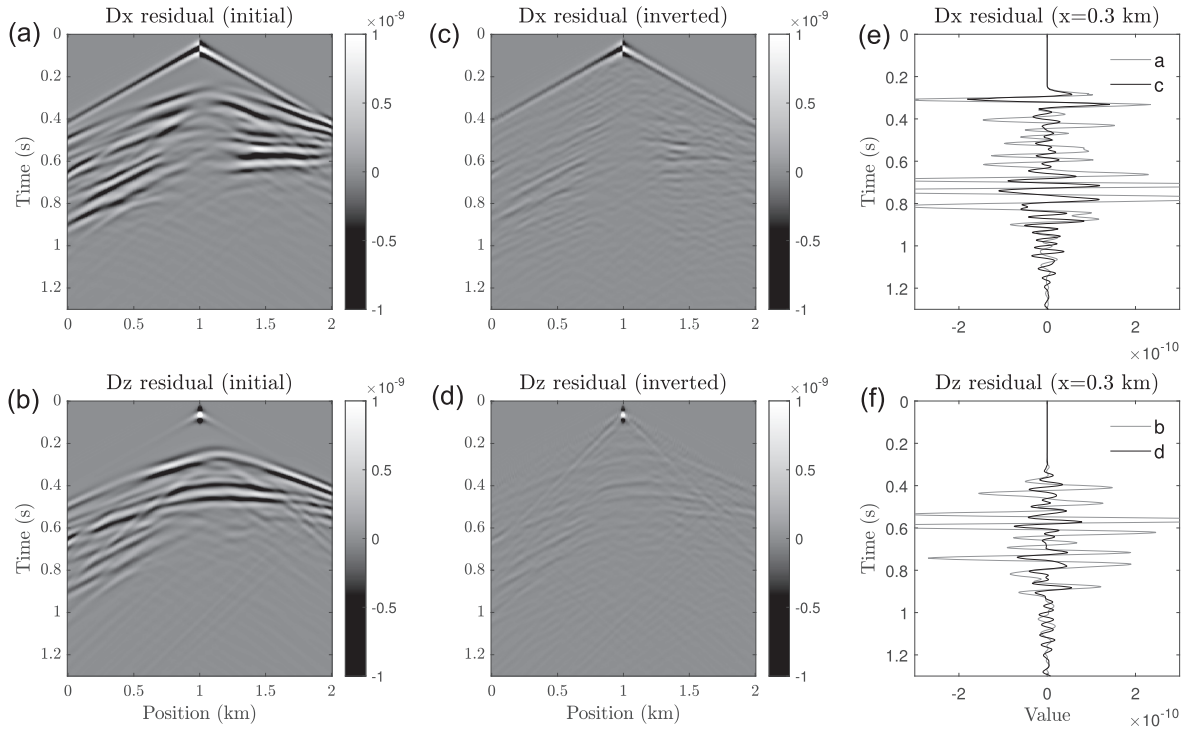
Figure 9. Baseline data residuals corresponding to the (a) and (b) initial model and (c) and (d) inverted model. (e) and (f) Vertical profiles of the data residuals at lateral position 0.3 km.
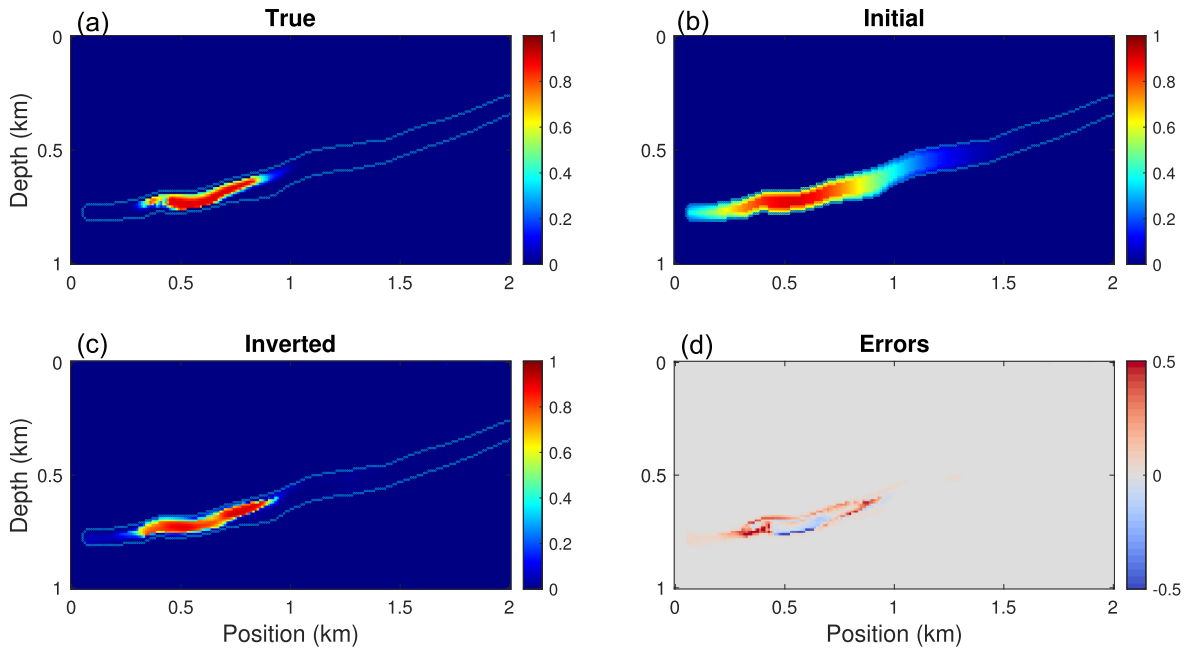

Figure 10. (a)–(c) True, initial and inverted CO_2 saturation models, respectively. (d) Errors in the inverted model.

model. The results are plotted in Figs 14 and 15. The velocity and density models are well recovered, but less accurately compared to the result of the rock physics FWI approach (Fig. 12), and the predicted time-lapse variations are contaminated by artefacts more seriously. We attribute this deficit to a slower convergence of the velocity-density parametrized FWI, when compared to that of the rock physics parametrized inversion, which results from the fact that more variables are inverted simultaneously.

We examine two approaches for the prediction of rock physics properties from velocities and density. One is a Bayesian non-parametric approach, in which the joint distribution of elastic and rock physics properties is described by a non-parametric probability density function estimated using kernel density estimation (Doyen 2007; Grana *et al.* 2021). We compute the joint distribution based on a training data set collected from wells and then use it to compute the conditional probability of rock physics variables given velocities and density. The most
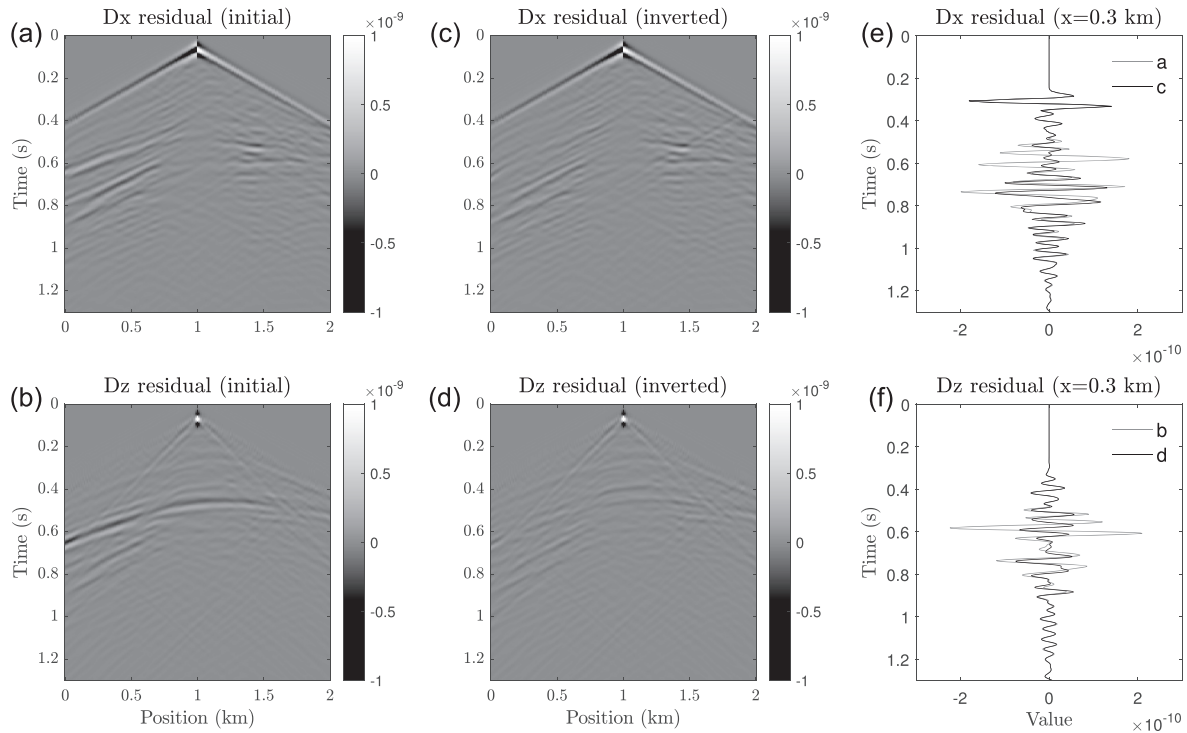
Figure 11. Monitor data residuals corresponding to the (a) and (b) initial model and (c) and (d) inverted model. (e) and (f) Vertical profiles of the data residuals at lateral position 0.3 km.
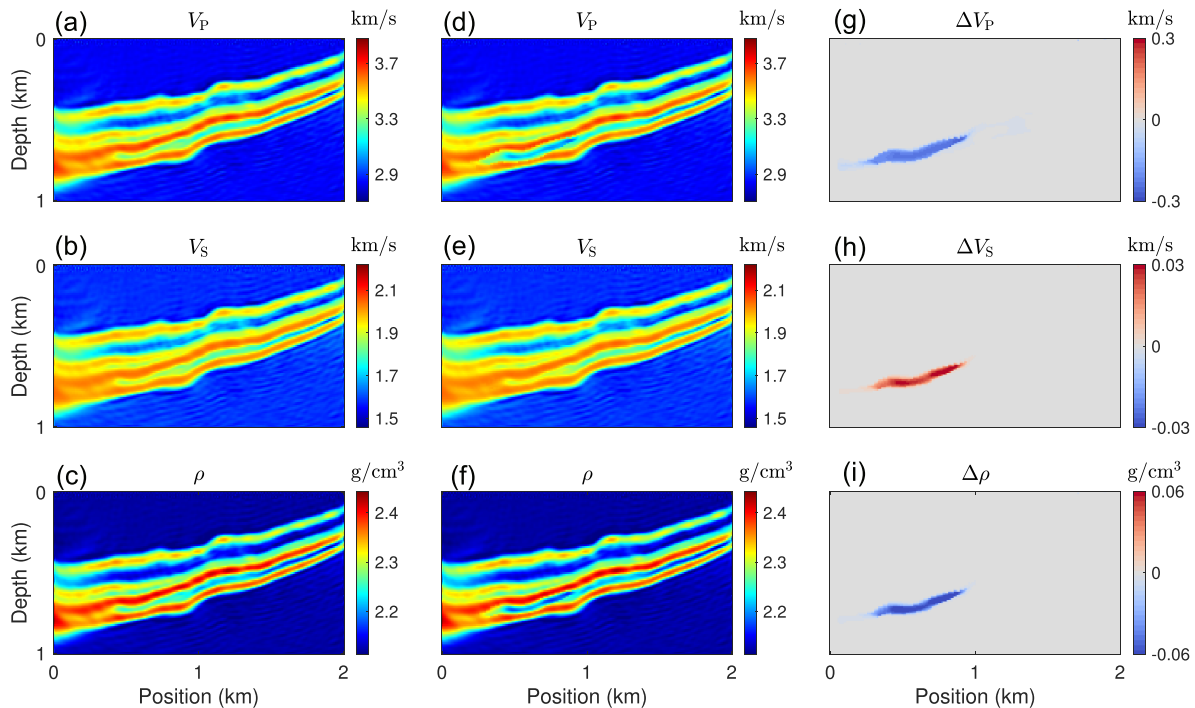

Figure 12. Reconstructed velocity and density models via the rock physics parametrized FWI: (a)–(c) baseline, (d)–(f) monitor and (g)–(i) time-lapse change.

likely model (i.e. maximum a posteriori estimate) is subsequently used for analysis. The other one is a global optimization method called the neighbourhood algorithm (NA), which involves random sampling of model space but makes use of previous samples to guide the search (Sambridge 1999; Sen & Roy 2003; Dupuy *et al.* 2016). For both approaches, we predict porosity and clay content from baseline velocity and density estimates, and CO_2 saturation from monitor estimates. Parameters in each inversion are tuned to provide robust results.

Fig. 16 shows that the two approaches yield comparable results of porosity and clay content to the direct inversion, capturing the relevant reservoir structures. The recovered CO_2 model is less than satisfactory, with the shape of the plume clearly distorted and the variation in
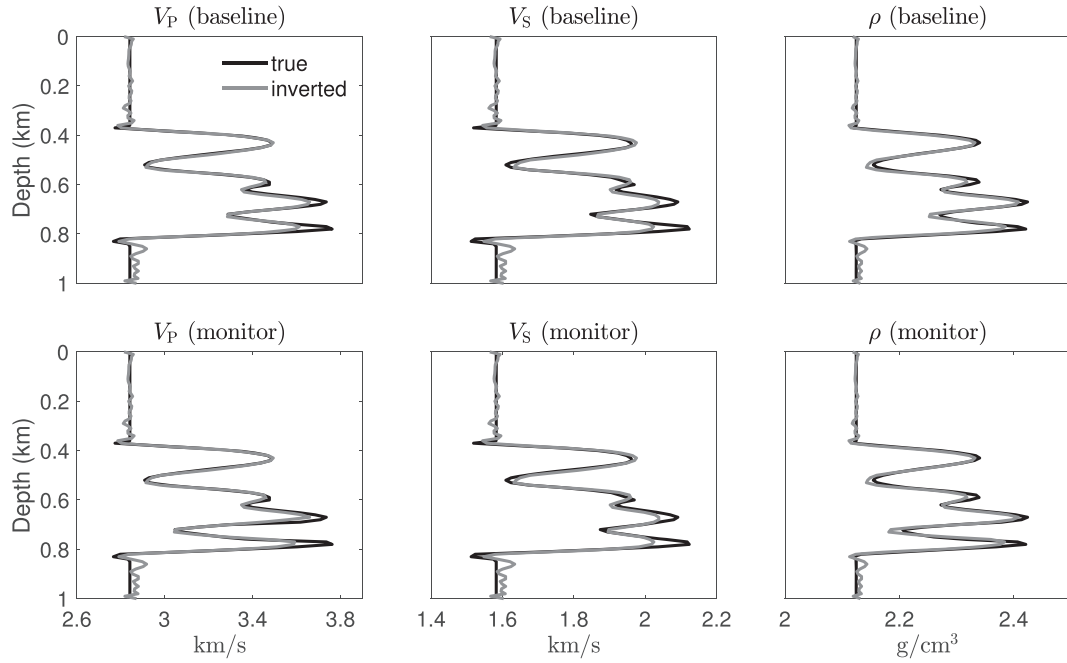
Figure 13. Vertical profiles extracted from the true and inverted models (Figs 3 and 12) at lateral position 0.5 km.
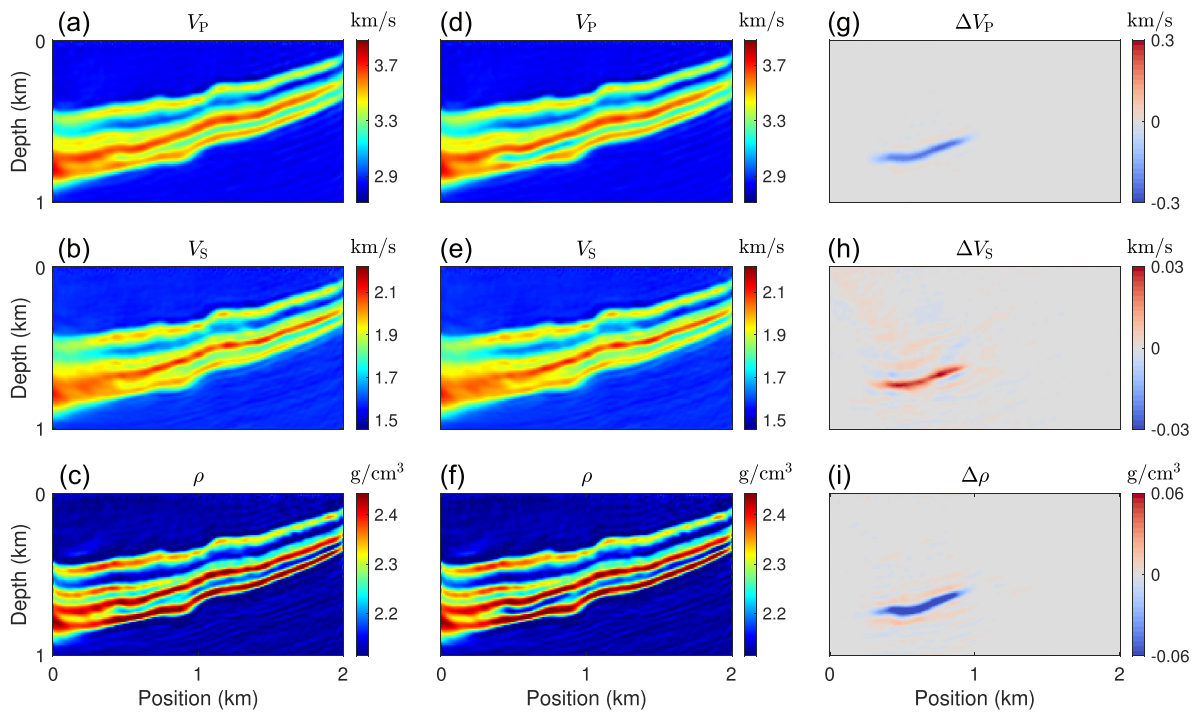

Figure 14. Reconstructed velocity and density models via velocity-density parametrized FWI: (a)–(c) baseline, (d)–(f) monitor and (g)–(i) time-lapse change.

saturation underestimated. Overall, the direct approach predicts CO_2 saturation more accurately (Fig. 10c). In Table 2, the quality of the inverted models within different approaches, measured using root mean squared error, is summarized.

3.4 Direct FWI with noisy data and imperfect rock physics model

To make the numerical study more realistic, we repeat the experiments in Section 3.2 considering two sources of uncertainty: uncertainty in the measured data owing to noise, and uncertainty in the rock physics model owing to the assumption of the way fluid phases are mixed. The two uncertainties are examined separately.
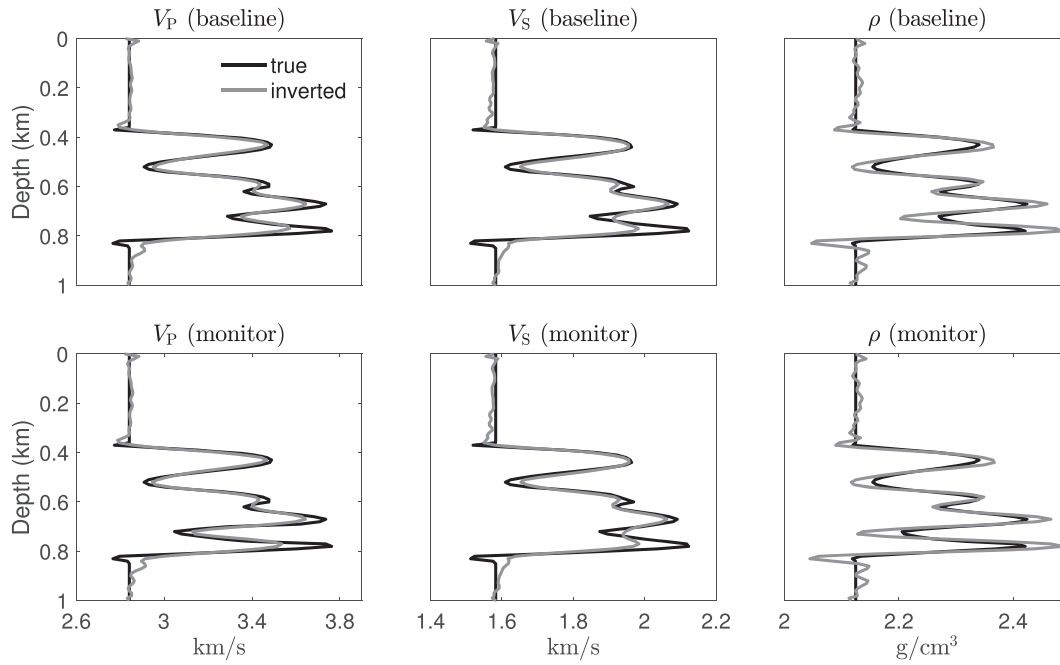
Figure 15. Vertical profiles extracted from the true and inverted models (Figs 3 and 14) at lateral position 0.5 km.
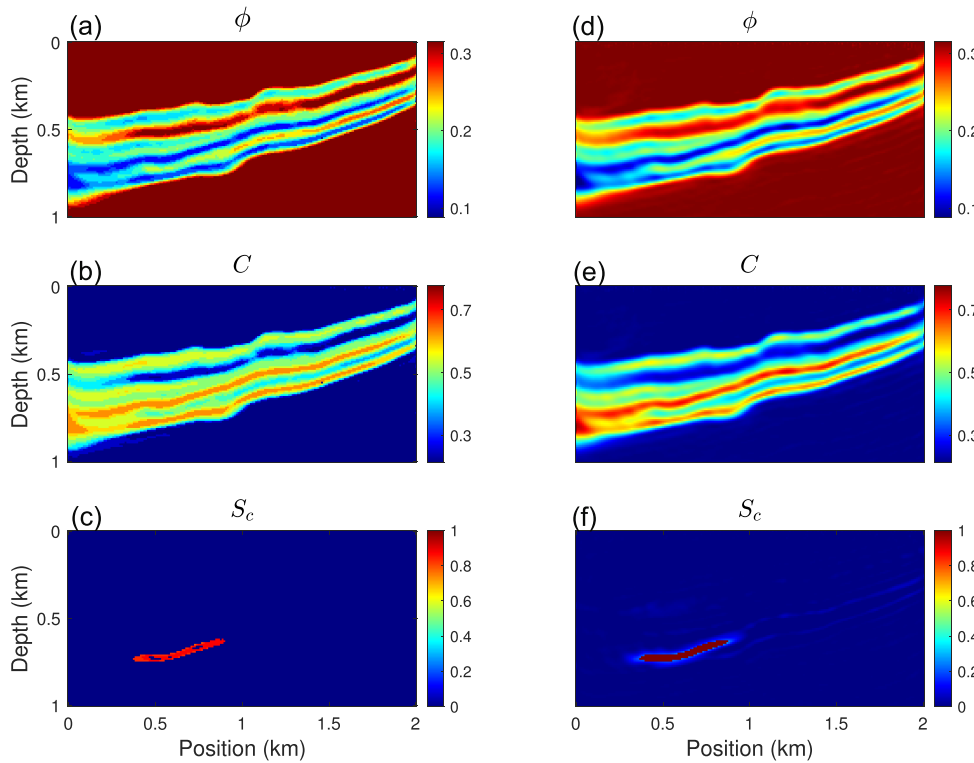

Figure 16. Inverted porosity, clay content and CO_2 saturation models within the (a)–(c) Bayesian and (d)–(f) NA approaches.

Table 2. Root mean squared error of the inverted models within different approaches.

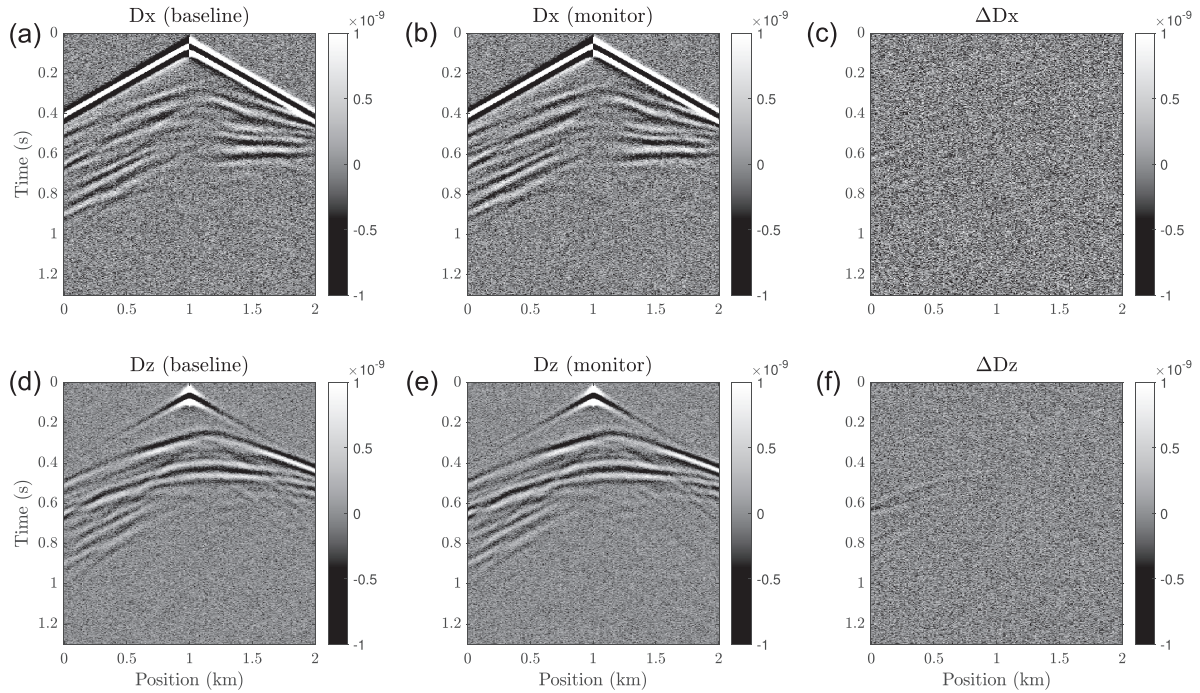|	FWI+Bayesian	FWI+NA	Direct FWI
V_P (km s^{-1}, base)	0.060	–	0.048
V_S (km s^{-1}, base)	0.040	–	0.033
ρ (g cm^{-3}, base)	0.022	–	0.015
V_P (km s^{-1}, monitor)	0.062	–	0.050
V_S (km s^{-1}, monitor)	0.040	–	0.033
ρ (g cm^{-3}, monitor)	0.023	–	0.016
ϕ	0.011	0.012	0.011
C	0.038	0.043	0.044
Sc	0.062	0.046	0.035

Figure 17. Synthetic noisy data with signal-to-noise ratio equal to 10.
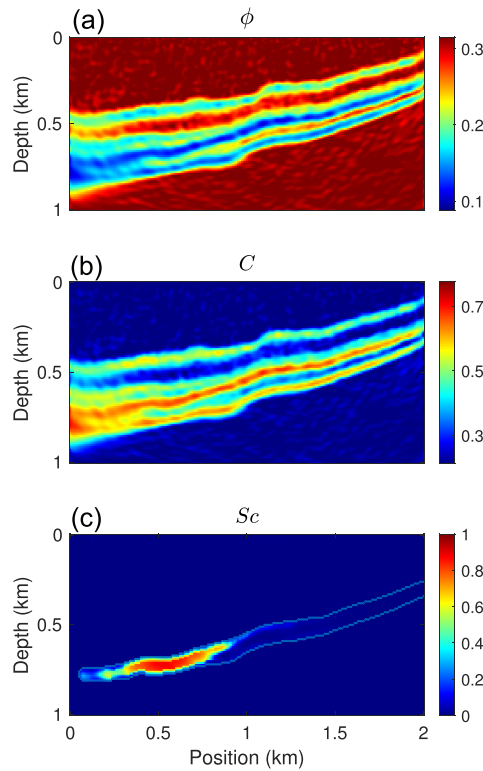

Figure 18. Direct inversion results with noisy data: (a) porosity, (b) clay content and (c) CO_2 saturation.

First, we add white Gaussian noise to the noise-free data (Fig. 4) using a signal-to-noise ratio of 10. As a result, the time-lapse seismic events are obscured by noise (Fig. 17). However, the inversion results (Fig. 18) remain consistent with the noise-free test, even though more noisy. The prediction error of porosity and clay content is larger toward the left side of the model due to the lack of illumination, and this likely cause data residuals that have been backprojected to the CO_2 estimate. Also, the sharpness of the recovered model is a bit degraded, indicating that the noise has impeded the convergence.
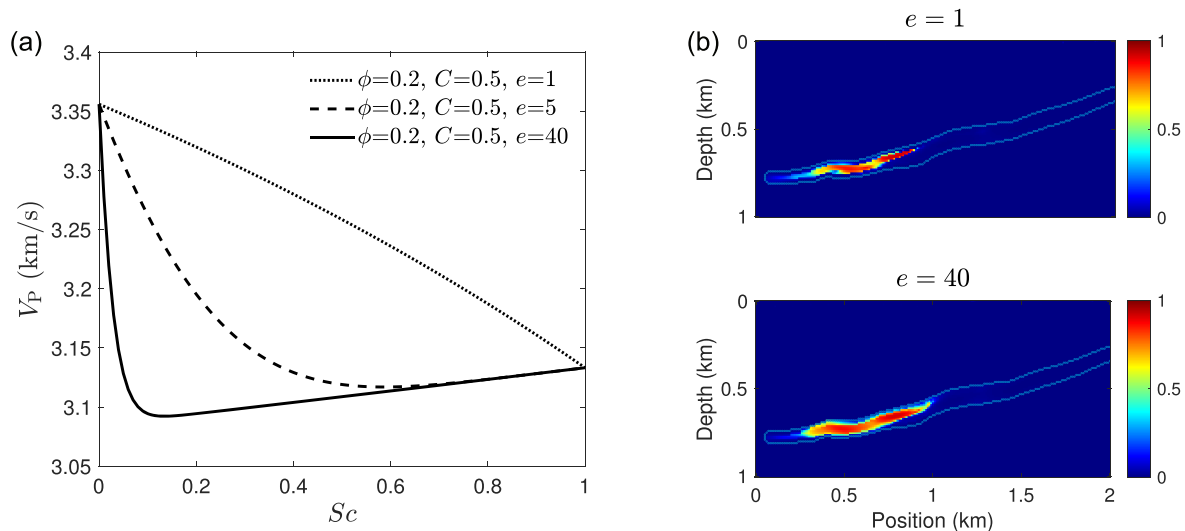
Figure 19. (a) *P*-wave velocity versus CO_2 saturation for different mixing behaviours of fluid phases. (b) Recovered CO_2 saturation models with erroneous assumptions on fluid.

We next consider an imperfect rock physics model that has errors on *a priori* parameter: the patchiness exponent *e* (eq. 17), which describes the way CO_2 and water are mixed in the pore space. In Fig. 19(a), we plot *P*-wave velocity as a function of CO_2 saturation, assuming patchy ($e = 1$), semi-patchy ($e = 5$) and uniform ($e = 40$) mixing behaviours, respectively, following the analysis of Dupuy *et al.* (2021b). It shows that the patchiness exponent has a large impact on *P*-wave velocity, especially when CO_2 saturation is low (but nonzero). To account for the uncertainty in the rock physics model, we generate the observed data using a patchiness exponent ($e = 1$ and 40) different from that used to compute the data in inversion ($e = 5$). The results are shown in Fig. 19(b). In the case of $e = 40$, we observe a similar result to the previous example, where the rock physics model is assumed perfect (Fig. 10c). This is attributed to the bimodality of the true model and the fact that the velocity difference between $e = 5$ and 40 at high CO_2 saturations ($Sc > 0.6$) is almost negligible. In the case of $e = 1$, the estimation error increases, but may still be considered as acceptable. Since the patchiness exponent only affects *P*-wave velocity, our interpretation is that the use of multicomponent elastic data helps to constrain the saturation estimation.

4 DISCUSSION

To validate the methodology some assumptions on the mineral and fluid phases were made. Indeed, we assume that the mineral phase consists of two minerals only and the fluid phase consists of water and CO_2. The methodology can be extended to more complex rocks as long as the elastic property of the minerals are known and the effective elastic properties can be modelled using rock physics elastic averages. Potentially the method can be applied in carbonate, however adequate rock physics models should be developed to account for the interaction of the fluid with fractured rocks (Vialle & Vanorio 2011; Vanorio 2015). Furthermore the approach could also be extended to a three-phase fluid system with water, oil and CO_2, to model CO_2 sequestration in oil reservoirs for enhanced oil recovery, but it requires some prior knowledge or assumptions on the initial fluid distribution.

In our simulation, the pressure variations are relatively small and we can assume that the effect of pressure changes on elastic properties and density is negligible. In case of larger variations, a joint rock physics model combining Gassmann's equations with empirical pressure relations (MacBeth 2004; Grana 2016b; Mavko *et al.* 2020) can be used as shown in Landrø *et al.* (2003), Trani *et al.* (2011), Bhakta & Landrø (2014) and Dupuy *et al.* (2021b). This approach requires adding one degree of freedom for pressure variations in the inversion.

The local smoothness is not always desirable, because it causes an attenuation of the high wavenumbers present in the model. In the CO_2 case, we found this constraint helpful in reducing undesired discontinuities and driving the convergence towards geologically meaningful models. However, one needs to weight the smoothness carefully to keep the level of details expected in an FWI result.

As a local inversion method, FWI bears the danger to end up in one of the numerous local minima. A good initial model is required to mitigate this problem. In practice, the initial porosity and clay content models can be obtained using some geostatistical interpolation of filtered logs following the seismically interpreted horizons, and using some correlated variable such as stacking velocities. The initial CO_2 model can be generated by simulating the fluid flow in the aquifer, according to the injection parameters and the rock properties estimated from the baseline survey (Grana *et al.* 2021).

Geophysical reservoir monitoring can be integrated in history matching and data assimilation workflows (Tavakoli *et al.* 2013; Ghorbanidehno *et al.* 2015) by combining the information from geophysical modelling with dynamic fluid flow simulation to increase the accuracy of the predicted model during injection and reduce the uncertainty in the model predictions (Chen *et al.* 2020; Liu & Grana 2020; Tveit *et al.* 2020). This approach is particularly useful for CO_2 sequestration and enhanced oil recovery studies where production data such as oil

production and borehole pressure can be used to validate and update the reservoir model (Babak & Deutsch 2008; Jahangiri & Zhang 2012; Gao *et al.* 2016; Kamali *et al.* 2017).

The inversion code is written in MATLAB. The computational cost for the proposed model including 101×201 grid cells with three unknown variables at each location for a total of 60 903 unknowns is approximately 1.5 hr, with a coarse parallelization over frequencies on a computer with an Intel Core i5-8600 3.10GHz processor. We note that the computational cost of this problem is about the same per iteration as for a conventional EFWI because the additional cost for parametrization is negligible. For large-scale field data applications, we recommend implementing this algorithm in a precompiled language and using massive parallelization on high-performance computers.

5 CONCLUSION

We present a quantitative CO_2 monitoring approach which is based on seismic FWI. Unlike conventional FWI approaches which aim at determination of elastic properties, the proposed scheme allows direct prediction of rock physics properties from seismic data. We propose to estimate rock frame properties, such as porosity and clay content, from baseline data (before CO_2 injection), and then use the results as input to estimate CO_2 saturation from monitor data. The method was tested on a synthetic model developed from the Johansen data set. With a suitable initial model, the method exhibits higher prediction accuracy than conventional two-step approaches. However, the difference between the direct and two-step inversions remains methodological and depends on the availability of sufficient constraints to the inversion. The results with noisy data and erroneous rock physics model further verify the robustness of the direct approach. The proposed methodology was applied to a saline aquifer but could be extended to depleted hydrocarbon reservoirs as well as enhanced oil recovery and carbon capture, utilization and storage (CCUS) applications.

DATA AVAILABILITY

The data used in this paper are available in its online Supporting Information.

REFERENCES

Alemie, W.M., 2017. *Time-Lapse Full Waveform Inversion Methods,* PhD thesis, Alberta University.

Arts, R., Eiken, O., Chadwick, A., Zweigel, P., Van der Meer, L. & Zinszner, B., 2003. Monitoring of CO₂ injected at Sleipner using time lapse seismic data, *Greenhouse Gas Control Technologies-6th International Conference,* pp. 347–352, Elsevier.

Asnaashari, A., Brossier, R., Garambois, S., Audebert, F., Thore, P. & Virieux, J., 2013. Regularized seismic full waveform inversion with prior model information, *Geophysics,* **78**(2), R25–R36.

Asnaashari, A., Brossier, R., Garambois, S., Audebert, F., Thore, P. & Virieux, J., 2015. Time-lapse seismic imaging using regularized full-waveform inversion with a prior model: which strategy?, *Geophys. Prospect.,* **63**(1), 78–98.

Babak, O. & Deutsch, C., 2008. Simulating oil recovery during CO₂ sequestration into a mature oil reservoir, *J. Canadian Petrol. Technol.,* **47**(08), 34–40.

Bergmo, P. E.S., Grimstad, A.-A. & Lindeberg, E., 2011. Simultaneous CO₂ injection and water production to optimise aquifer storage capacity, *Int. J. Greenhouse Gas Contr.,* **5**(3), 555–564.

Bhakta, T. & Landrø, M., 2014. Estimation of pressure-saturation changes for unconsolidated reservoir rocks with high Vp/Vs ratio, *Geophysics,* **79**(5), M35–M54.

Bosch, M., Cara, L., Rodrigues, J., Navarro, A. & Díaz, M., 2007. A Monte Carlo approach to the joint estimation of reservoir and elastic parameters from seismic amplitudes, *Geophysics,* **72**(6), O29–O39.

Bosch, M., Mukerji, T. & Gonzalez, E.F., 2010. Seismic inversion for reservoir properties combining statistical rock physics and geostatistics: a review, *Geophysics,* **75**(5), 75A165–75A176.

Brie, A., Pampuri, F., Marsala, A. & Meazza, O., 1995. Shear sonic interpretation in gas-bearing sands, in *SPE Annual Technical Conference and Exhibition,* OnePetro.

Brossier, R., Operto, S. & Virieux, J., 2009. Seismic imaging of complex onshore structures by 2D elastic frequency-domain full-waveform inversion, *Geophysics,* **74**(6), WCC105–WCC118.

Bunks, G., Saleck, F.M., Zaleski, S. & Chavent, G., 1995. Multiscale seismic waveform inversion, *Geophysics,* **60**(5), 1457–1473.

Chadwick, R., Arts, R. & Eiken, O., 2005. 4D seismic quantification of a growing CO₂ plume at Sleipner, North Sea, in *Geological Society, London, Petroleum Geology Conference Series,* Vol. **6,** pp. 1385–1399, Geological Society of London.

Chen, B., Harp, D.R., Lu, Z. & Pawar, R.J., 2020. Reducing uncertainty in geologic CO₂ sequestration risk assessment by assimilating monitoring data, *Int, J. Greenhouse Gas Contr.,* **94,** 102926.

Davis, T.L., Landrø, M. & Wilson, M., 2019. *Geophysics and Geosequestration,* Cambridge University Press.

De Barros, L. & Dietrich, M., 2008. Perturbations of the seismic reflectivity of a fluid-saturated depth-dependent poroelastic medium, *J. acoust. Soc. Am.,* **123**(3), 1409–1420.

Doyen, P., 2007. *Seismic Reservoir Characterization: An Earth modelling perspective,* EAGE Publications.

Dupuy, B., Garambois, S. & Virieux, J., 2016. Estimation of rock physics properties from seismic attributes—Part 1: Strategy and sensitivity analysis, *Geophysics,* **81**(3), M35–M53.

Dupuy, B., Romdhane, A., Eliasson, P., Querendez, E., Yan, H., Torres, V.A. & Ghaderi, A., 2017. Quantitative seismic characterization of co2 at the sleipner storage site, north sea, *Interpretation,* **5**(4), SS23–SS42.

Dupuy, B., Romdhane, A., Eliasson, P. & Yan, H., 2021a. Combined geophysical and rock physics workflow for quantitative CO_2 monitoring, *Int. J. Greenhouse Gas Contr.,* **106,** 103217.

Dupuy, B., Romdhane, A., Nordmann, P.-L., Eliasson, P. & Park, J., 2021b. Bayesian rock-physics inversion: application to co2 storage monitoring, *Geophysics,* **86**(4), M101–M122.

Eigestad, G.T., Dahle, H.K., Hellevang, B., Riis, F., Johansen, W.T. & Øian, E., 2009. Geological modeling and simulation of CO_2 injection in the Johansen formation, *Comput. Geosci.,* **13**(4), 435–450.

Fu, X., Romahn, S. & Innanen, K., 2020. Double-wavelet double-difference time-lapse waveform inversion, in *SEG Technical Program Expanded Abstracts 2020,* pp. 3764–3767, Society of Exploration Geophysicists.

Furre, A.-K., Kiær, A. & Eiken, O., 2015. Co2-induced seismic time shifts at sleipner, *Interpretation,* **3**(3), SS23–SS35.

Gao, R.S., Sun, A.Y. & Nicot, J.-P., 2016. Identification of a representative dataset for long-term monitoring at the Weyburn CO_2-injection enhanced oil recovery site, Saskatchewan, Canada, *Int. J. Greenhouse Gas Contr.,* **54,** 454–465.

Ghorbanidehno, H., Kokkinaki, A., Li, J.Y., Darve, E. & Kitanidis, P.K., 2015. Real-time data assimilation for large-scale systems: The spectral Kalman filter, *Adv. Water Resour.,* **86,** 260–272.

Ghosh, R., Sen, M.K. & Vedanti, N., 2015. Quantitative interpretation of CO_2 plume from Sleipner (North Sea), using post-stack inversion and rock physics modeling, *Int. J. Greenhouse Gas Contr.,* **32,** 147–158.

Grana, D., 2016a. Bayesian linearized rock-physics inversion, *Geophysics,* **81**(6), D625–D641.

Grana, D., 2016b. Pressure–velocity relations in reservoir rocks: Modified MacBeth's equation, *J. Appl. Geophys.,* **132,** 234–241.

Grana, D., Liu, M. & Ayani, M., 2020. Prediction of CO_2 saturation spatial distribution using geostatistical inversion of time-lapse geophysical data, *IEEE Trans. Geosci. Remote Sens.,* **59**(5), 3846–3856.

Grana, D., Mukerji, T. & Doyen, P., 2021. *Seismic Reservoir Modeling: Theory, Examples, and Algorithms,* John Wiley & Sons.

Grude, S., Landrø, M. & Osdal, B., 2013. Time-lapse pressure–saturation discrimination for CO_2 storage at the Snøhvit field, *Int. J. Greenhouse Gas Contr.,* **19,** 369–378.

Hill, R., 1952. The elastic behaviour of a crystalline aggregate, *Proc. Phys. Soc. A,* **65**(5), 349–354.

Hossain, Z., Mukerji, T., Dvorkin, J. & Fabricius, I.L., 2011. Rock physics model of glauconitic greensand from the North Sea, *Geophysics,* **76**(6), E199–E209.

Hu, Q. & Innanen, K., 2021. Elastic full-waveform inversion with rock-physics constraints, in *First International Meeting for Applied Geoscience & Energy,* pp. 662–666, Society of Exploration Geophysicists.

Hu, Q., Keating, S., Innanen, K.A. & Chen, H., 2021. Direct updating of rock-physics properties using elastic full-waveform inversion, *Geophysics,* **86**(3), MR117–MR132.

Jahangiri, H.R. & Zhang, D., 2012. Ensemble based co-optimization of carbon dioxide sequestration and enhanced oil recovery, *Int. J. Greenhouse Gas Contr.,* **8,** 22–33.

Johnston, D.H., 2013. *Practical Applications of Time-lapse Seismic Data,* Society of Exploration Geophysicists.

Kamali, F., Hussain, F. & Cinar, Y., 2017. An experimental and numerical analysis of water-alternating-gas and simultaneous-water-and-gas displacements for carbon dioxide enhanced oil recovery and storage, *SPE J.,* **22**(02), 521–538.

Kamei, R. & Lumley, D., 2017. Full waveform inversion of repeating seismic events to estimate time-lapse velocity changes, *J. geophys. Int.,* **209**(2), 1239–1264.

Keating, S. & Innanen, K.A., 2019. Parameter crosstalk and modeling errors in viscoacoustic seismic full-waveform inversion, *Geophysics,* **84**(4), R641–R653.

Keating, S. & Innanen, K.A., 2020. Parameter crosstalk and leakage between spatially separated unknowns in viscoelastic full-waveform inversion, *Geophysics,* **85**(4), R397–R408.

Landrø, M., Veire, H.H., Duffaut, K. & Najjar, N., 2003. Discrimination between pressure and fluid saturation changes from marine multicomponent time-lapse seismic data, *Geophysics,* **68**(5), 1592–1599.

Liu, M. & Grana, D., 2018. Stochastic nonlinear inversion of seismic data for the estimation of petroelastic properties using the ensemble smoother and data reparameterization, *Geophysics,* **83**(3), M25–M39.

Liu, M. & Grana, D., 2020. Petrophysical characterization of deep saline aquifers for CO_2 storage using ensemble smoother and deep convolutional autoencoder, *Adv. Water Resour.,* **142,** 103634.

MacBeth, C., 2004. A classification for the pressure-sensitivity properties of a sandstone rock frame, *Geophysics,* **69**(2), 497–510.

Maharramov, M., Biondi, B. & Meadows, M., 2016. Time-lapse inverse theory with applications, *Geophysics,* **81,** R485–R501.

Mallick, S. & Adhikari, S., 2015. Amplitude-variation-with-offset and prestack-waveform inversion: a direct comparison using a real data example from the Rock Springs Uplift, Wyoming, USA, *Geophysics,* **80**(2), B45–B59.

Mavko, G., Mukerji, T. & Dvorkin, J., 2020. *The Rock Physics Handbook,* Cambridge University Press.

Métivier, L., Brossier, R., Operto, S. & Virieux, J., 2017. Full waveform inversion and the truncated Newton method, *SIAM Rev.,* **59**(1), 153–195.

Morency, C., Luo, Y. & Tromp, J., 2009. Finite-frequency kernels for wave propagation in porous media based upon adjoint methods, *J. geophys. Int.,* **179**(2), 1148–1168.

Operto, S., Gholami, Y., Prieux, V., Ribodetti, A., Brossier, R., Metivier, L. & Virieux, J., 2013. A guided tour of multiparameter full-waveform inversion with multicomponent data: From theory to practice, *Leading Edge,* **32**(9), 1040–1054.

Pan, W.Y., Innanen, K.A., Geng, Y. & Li, J.X., 2019. Interparameter trade-off quantification for isotropic-elastic full-waveform inversion with various model parameterizations, *Geophysics,* **84**(2), R185–R206.

Plessix, R.-E., Michelet, S., Rynja, H., Kuehl, H., Perkins, C., de Maag, J. & Hatchell, P., 2010. Some 3d applications of full waveform inversion, in *72nd EAGE Conference and Exhibition-Workshops and Fieldtrips,* pp. cp–162, European Association of Geoscientists & Engineers.

Pörtner, H.O. *et al.*, 2022. *Climate Change 2022: Impacts, Adaptation and Vulnerability,* Contribution of Working Group II to the Sixth Assessment Report of the Intergovernmental Panel on Climate Change, Cambridge University Press. Cambridge University Press, Cambridge, UK and New York, NY.

Pratt, R.G., 1990. Frequency-domain elastic wave modeling by finite differences: a tool for crosshole seismic imaging, *Geophysics,* **55**(5), 626–632.

Prieux, V., Brossier, R., Operto, S. & Virieux, J., 2013. Multiparameter full waveform inversion of multicomponent ocean-bottom-cable data from the Valhall field. Part 1: Imaging compressional wave speed, density and attenuation, *J. geophys. Int.,* **194**(3), 1640–1664.

Queißer, M. & Singh, S.C., 2013a. Full waveform inversion in the time lapse mode applied to CO_2 storage at Sleipner, *Geophys. Prospect.,* **61**(3), 537–555.

Queißer, M. & Singh, S.C., 2013b. Localizing CO_2 at Sleipner-seismic images versus P-wave velocities from waveform inversion, *Geophysics,* **78**(3), B131–B146.

Ringrose, P., 2020. *How to Store CO_2 Underground: Insights from Early-mover CCS Projects,* Springer.

Roach, L.A., White, D.J. & Roberts, B., 2015. Assessment of 4D seismic repeatability and CO_2 detection limits using a sparse permanent land array at the aquistore CO_2 storage site, *Geophysics,* **80**(2), WA1–WA13.

Romdhane, A. & Querendez, E., 2014. CO_2 characterization at the Sleipner field with full waveform inversion: application to synthetic and real data, *Energy Proced.,* **63,** 4358–4365.

Russell, B.H., Gray, D. & Hampson, D.P., 2011. Linearized AVO and poroelasticity, *Geophysics,* **76**(3), C19–C29.

Rütters, H. *et al.*, 2013. State-of-the-art of monitoring methods to evaluate storage site performance, *CGS Europe Key Report,* **1,** 109.

Sambridge, M., 1999. Geophysical inversion with a neighbourhood algorithm—I. searching a parameter space, *J. geophys. Int.,* **138**(2), 479–494.

Sen, M.K. & Roy, I.G., 2003. Computation of differential seismograms and iteration adaptive regularization in prestack waveform inversion, *Geophysics,* **68**(6), 2026–2039.

Shulakova, V., Pevzner, R., Dupuis, J.C., Urosevic, M., Tertyshnikov, K., Lumley, D.E. & Gurevich, B., 2015. Burying receivers for improved time-lapse seismic repeatability: CO_2CRC otway field experiment, *Geophys. Prospect.,* **63**(1), 55–69.

Spikes, K., Mukerji, T., Dvorkin, J. & Mavko, G., 2007. Probabilistic seismic inversion based on rock-physics models, *Geophysics,* **72**(5), R87–R97.

Tarantola, A., 1986. A strategy for nonlinear elastic inversion of seismic reflection data, *Geophysics,* **51**(10), 1893–1903.

Tavakoli, R., Yoon, H., Delshad, M., ElSheikh, A.H., Wheeler, M.F. & Arnold, B.W., 2013. Comparison of ensemble filtering algorithms and null-space Monte Carlo for parameter estimation and uncertainty quantification using CO_2 sequestration data, *Water Resour. Res.,* **49**(12), 8108–8127.

Tikhonov, A.N. & Arsenin, V.Y., 1977. Solutions of ill-posed problems, *Winston and Sons,* New York.

Trani, M., Arts, R., Leeuwenburgh, O. & Brouwer, J., 2011. Estimation of changes in saturation and pressure from 4D seismic AVO and time-shift analysis, *Geophysics,* **76**(2), C1–C17.

Tveit, S., Mannseth, T., Park, J., Sauvin, G. & Agersborg, R., 2020. Combining CSEM or gravity inversion with seismic AVO inversion, with application to monitoring of large-scale CO_2 injection, *Comput. Geosci.,* **24**(3), 1201–1220.

Vanorio, T., 2015. Recent advances in time-lapse, laboratory rock physics for the characterization and monitoring of fluid-rock interactions, *Geophysics,* **80**(2), WA49–WA59.

Vialle, S. & Vanorio, T., 2011. Laboratory measurements of elastic properties of carbonate rocks during injection of reactive CO_2-saturated water, *Geophys. Res. Lett.,* **38**(1).

Virieux, J. & Operto, S., 2009. An overview of full-waveform inversion in exploration geophysics, *Geophysics,* **74**(6), WCC1–WCC26.

Wawrzyniak-Guz, K., 2019. Rock physics modelling for determination of effective elastic properties of the lower Paleozoic shale formation, North Poland, *Acta Geophys.,* **67**(6), 1967–1989.

Yang, Q., Malcolm, A., Rusmanugroho, H. & Mao, W., 2019. Analysis of radiation patterns for optimized full waveform inversion in fluid-saturated porous media, *J. geophys. Int.,* **216**(3), 1919–1937.

Zhang, F., Juhlin, C., Ivandic, M. & Lüth, S., 2013. Application of seismic full waveform inversion to monitor CO_2 injection: modelling and a real data example from the Ketzin site, Germany, *Geophys. Prospect.,* **61**, 284–299.

SUPPORTING INFORMATION

Supplementary data are available at *GJI* online.

suppl_data

Please note: Oxford University Press is not responsible for the content or functionality of any supporting materials supplied by the authors. Any queries (other than missing material) should be directed to the corresponding author for the paper.